Modeling of Gas Diffusion in Ni/YSZ Electrodes in CO2 and Co-electrolysis

Duhn, Jakob Dragsbæk; Jensen, Anker Degn; Wedel, Stig; Wix, Christian

Published in:
Fuel Cells

Link to article, DOI:
10.1002/fuce.201700068

Publication date:
2017

Document Version
Peer reviewed version

Modelling of Gas Diffusion in Ni/YSZ Electrodes in CO_2 and co-electrolysis

Jakob Dragsbæk Duhn[1*], Anker Degn Jensen[1], Stig Wedel[1], Christian Wix[2]
[1]DTU Chemical Engineering, Søltofts Plads 229, 2800 Kgs. Lyngby/Denmark
[2]Haldor Topsoe A/S; Haldor Topsøes Allé 1, 2800 Kgs. Lyngby/Denmark
[*] Corresponding author: jadu@kt.dtu.dk

Abstract

Carbon formation may occur during CO_2 and CO_2/H_2O electrolysis using solid oxide electrolyzer cells due to the Boudouard reaction ($2CO \rightarrow CO_2 + C(s)$). Formed carbon may disintegrate the cell structure and it is therefore of importance to be able to predict when carbon is formed, and take actions to prevent its formation.
For prediction of carbon formation, the gas composition in the electrode must be known. In this work, the diffusion of gases in the electrode has been modelled with the dusty gas model in 1 and 2 dimensions, and the effect of tortuosity, porosity, temperature, electrode thickness, pore diameter, current density, pitch and rib width has been investigated. It is shown that diffusion limitations on reactant/product transport may lead to carbon formation.

The parameters describing the microstructure and the dimensions of the cathode channels and interconnect ribs are found to have a large effect on the carbon formation propensity. Given a set of parameters, a simple correlation between the CO mole fraction in the channel and under the interconnect rib, and current density during CO_2-electrolysis can be derived. This correlation makes it possible to efficiently integrate the calculation of carbon formation risk in existing electrolyzer cell models.

Keywords: Boudouard reaction, Carbon Formation, Diffusive Mass Transport, Electrolysis, Fuel cell, Mathematical Modeling, Solid Oxide Electrolysis Cell.

1 Introduction

Solid oxide electrolyzer cells (SOEC) are electrochemical devices capable of converting H_2O and CO_2 to H_2 and CO. The electrolysis of H_2O and CO_2 is important since it is capable of producing H_2, CO or syngas directly from electrical energy from e.g. renewable energy sources. These compounds can be used to produce synthetic hydrocarbon fuels as a solution to reduce oil consumption and carbon dioxide emissions.

However, the formation of carbon has been observed during electrolysis of CO_2 and CO_2 and H_2 co-electrolysis [1,2]. The carbon can block pores and reaction sites [3], cause the Ni structure in the electrode to change [4], and cause local fractures in the cermet [5]. It is therefore of great importance to avoid carbon formation. During both CO_2 and co-electrolysis carbon formation has been observed at operating conditions where it should be thermodynamically unfavored based on the gas composition in the bulk of the gas phase (i.e. in the gas channels of a stack) [2,6]. In the literature it has been presumed that this is caused by diffusion limitations within the electrode [2,6]. In this study we investigate this presumption by calculating the concentration profiles in the electrode and evaluate the risk of carbon formation based on the actual gas composition in the electrode, rather than the composition in the gas bulk.

Different models for diffusion in the electrode material have been used in the literature, including Fick's law, Stefan-Maxwell model, dusty gas model, binary friction model, and the cylindrical pore interpolation model [7–9]. The most frequently used models are Fick's law and dusty gas model [9]. Suwanwarangkul et al. [10] compared the performance of Fick's law, the Stefan-Maxwell model, and the dusty gas model in predicting the experimental measured concentration overpotentials in SOFC anodes for H_2-H_2O-Ar and CO-CO_2 systems. The concentration overpotential depends on the gas concentrations in both the gas channel and at the interface between the electrode and electrolyte. With the diffusion models, the gas composition at the interface can be calculated and thus also the concentration overpotential can be calculated and compared to the measured value.
Using this approach, Suwanwarangkul et al. [10] found that the dusty gas model was better at predicting the concentration overpotential. For the CO-CO_2 system Fick's law could also be used to model the system with acceptable accuracy (within 15 % of the results obtained by the dusty gas model) when the current density was low (0.1 A cm^{-2}) and at low (25 %) to intermediate (40%) CO concentrations. At a higher current density (0.3 A cm^{-2}) Fick's law could only be used for intermediate CO concentrations. Suwanwarangkul et al. [10] also found that the dusty gas model was the only suitable model for the H_2-H_2O-CO-CO_2 system. Vural et al. [8] found that the dusty gas model, Stefan-Maxwell model and the binary friction model all gave similar predictions for the concentration overpotential for H_2-H_2O-Ar and CO-CO_2 systems up to high current densities (1.5 A cm^{-2}) and small pore radius (0.27 µm). Wang et al. [11] compared the dusty gas model with the binary friction model and the cylindrical pore interpolation model and found that they gave similar results. In this study, the diffusion has been modelled with the dusty gas model. This model was chosen because 1) the investigated situations span a wide range of current density and CO concentrations, 2) the H_2-H_2O-CO-CO_2 system is also investigated.

Ni containing catalysts are used in different industrial processes such as reforming and high temperature methanation. The carbon formation on Ni has therefore been thoroughly studied [3,12–16]. Carbonaceous gas species might form solid carbon through the Boudouard reaction (Reaction 1) and methane decomposition (Reaction 2) [3,17]. The carbon can be in the form of graphite [18], pyrolytic carbon, carbides [19,20], and

filamentous carbon (also called whisker carbon) [14,21]. At the high temperatures used in SOECs, filamentous carbon and graphite will be formed [22,23], see Figure 1.

Boudouard reaction $2CO \rightleftharpoons CO_2+C(s)$ (1)

Methane decomposition $CH_4 \rightleftharpoons 2H_2+C(s)$ (2)

When both carbon and hydrogen species are present, the water-gas shift reaction and methanation reaction will also take place.

Water-gas shift $CO+H_2O \rightleftharpoons CO_2+H_2$ (3)
Methanation reactions $CO+3H_2 \rightleftharpoons CH_4+H_2O$ (4)

Carbon deposition on solid oxide cells running in fuel cell mode, with methane [23,24] and other hydrocarbons [25] as the carbon source, has been widely studied. However, only a few studies have focused on solid oxide cells running in electrolysis mode with either H_2O+CO_2 or CO_2 as the process feed [26–29]. In co-electrolysis carbon deposition has been observed and is believed to cause delamination of the electrode from the solid electrolyte after long-time testing (≤ 700 hr.) [1]. In CO_2-electrolysis it has been observed that just crossing the equilibrium (forming small amounts of carbon) is a reversible process [2]. It is generally accepted that carbon formation is to be expected when there is a nickel catalyst present and the gas shows affinity for carbon formation after the establishment of methanation and shift equilibria [30]. The affinity for carbon formation, a_c, is given as the equilibrium constant, divided with the reaction quotient:

$$a_c = K_1/Q_1 \quad (5)$$

$$Q_1 = \frac{X_{CO_2}}{X_{CO}^2 p_t} \quad (6)$$

K_1 is the equilibrium constant for reaction 1, Q_1 is the reaction quotient, X is the mole fraction of CO_2 and CO, respectively, and p_t is the total pressure in atm.

When $a_c > 1$, the gas shows affinity for carbon formation. Since the equilibrium constant is a function of temperature, the temperature at which the gas mixture starts to show affinity to carbon formation via the Boudouard reaction, T_B, can be calculated. If the equilibrium temperature is less than the actual temperature, the formation of carbon is thermodynamically unfavorable and if the equilibrium temperature is above the actual temperature, the formation of carbon is thermodynamically favorable. Calculating the equilibrium temperature is advantageous since the necessary temperature increase to avoid carbon formation can easily be calculated as $T_B - T_{cell}$.

Some studies have used the thermodynamic data for graphite when calculating the equilibrium constant for the Boudouard reaction [1,31,32]. However, there is a significant difference between the thermodynamic data for graphite and filamentous carbon [13,14,33]. Figure 1 shows the equilibrium curves for carbide (Ni_3C), graphite and filamentous carbon. It can be seen that for temperatures above 650 °C, the equilibrium constant is higher for filamentous carbon than graphite. Thus, the gas mixture will show affinity to filamentous carbon, rather than graphite carbon, at a higher temperature. Since we want to investigate situations where the gas composition has just crossed the equilibrium, we will use the thermodynamic data for filamentous carbon, which are based

on experimental studies [3,13,14]. The studies present somewhat different values for the equilibrium constant. In this study we have used the thermodynamic data given by Rostrup-Nielsen [13], since they are based on experiments up to 700 °C, whereas the others are based on temperatures below 575 °C [3] and 627 °C [14], respectively.

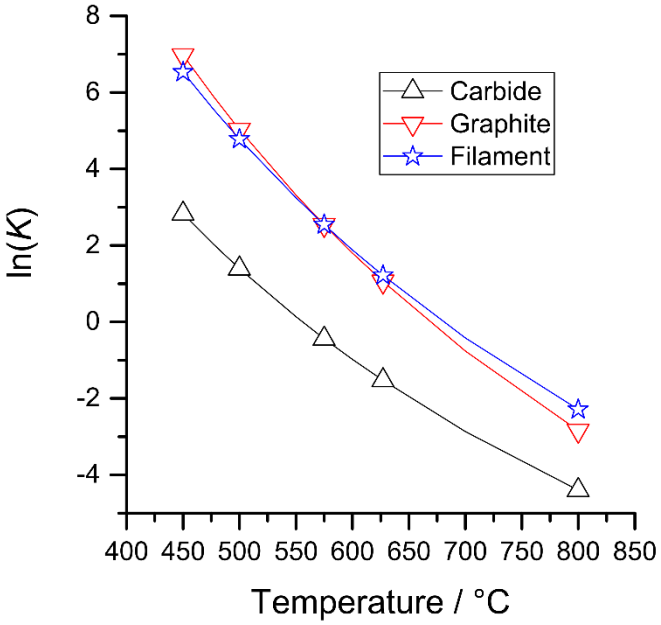

Figure 1. Equilibrium constant for different forms of carbon formation as function of temperature. Based on data from [3]**.**

2 Models

Figure 2a and 2b shows a schematic view of the SOEC. Starting from the top on figure 2a, gas is entering at the cathode gas channel and flows over the cathode. Gas species are diffusing through the porous cathode towards the electrode-electrolyte interface driven by a concentration gradient. At the electrode-electrolyte reaction interface the electrochemical reduction of CO_2 and H_2O takes place (reaction 14 and 15, see section 2.4). The thickness of this layer, d_i, is between a few µm and 20 µm [34–36]. In our modelling, we have selected a thickness of 10 µm. The specific number does not influence the results significantly, since the major part of the diffusion take place in the support layer, which is several times thicker than the reaction layer. The products of the electrochemical reactions, respectively CO and H_2, diffuse back to the channel and are swept out by the channel flow. During co-electrolysis, the water-gas shift reaction (reaction 3) as well as the methanation reaction (reaction 4) will also take place in the electrode.

The formed oxygen ions diffuse through the electrolyte and react to oxygen molecules at the anode. The formed oxygen molecules are transported out of the cell via the sweep flow in the anode channel. Figure 2b shows the cell in the x-z dimension, where the interconnect can be seen. The interconnect forms the cathode channels, which help distribute the fluid uniformly [37], and the rib, which ensures that there is electrical contact between adjacent cells.

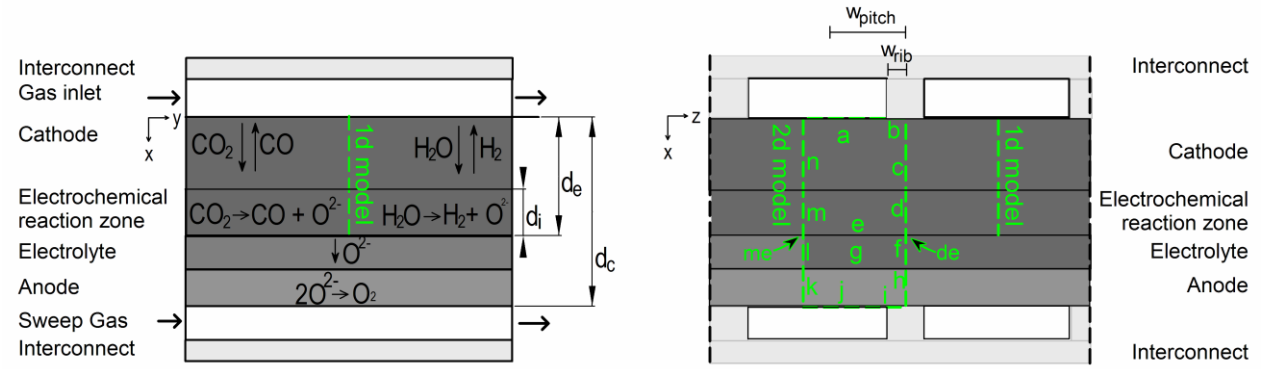

Figure 2a (left) and 2b (right). Figure 2a is a schematic xy-plane view of the cell and 2b is the a xz view of the cell. The 1d model is marked on both figures and the 2d model is marked on figure 2b. The single letters on figure 2b are used to label the boundaries and the double letters are used to label the points, which are referred to in the text.

Two models are used in this study: A 1d model and a 2d model (see figure 2a and 2b). The 1d model consists of the cathode and electrochemical reaction zone along the line shown in figure 2. The 2d model consists of the cathode, electrochemical reaction zone, electrolyte and anode (the rectangle shown in figure 2b). In the 2d model, the cathode and anode consist of parts with contact to the gas channel and with contact to the interconnect rib. In this way, the effect of the interconnect rib on the gas transfer and current density distribution is included. The letters in figure 2b are used to label the boundaries and are referred to in the following text. The point where “d” and “e” intersect (the point under the center of the rib) is labelled “de” in the following text. Likewise, the point where “m” and “e” intersect (the point under the center of the channel) is labelled “me”

The governing equations for both models are given in the following. The 1d model only considers the changes in the x direction and 2d model only considers the changes in the x and z direction.

The following assumptions have been made: 1) the total pressure in the channel is 1 atm, 2) the system is at steady state, 3) the part of the cell that is modeled is at isothermal conditions, 4) the material is isotropic, 5) the surface diffusion and thermal diffusion can be neglected. The assumption of isothermal condition is justified since the thickness of the cell is relatively thin and the thermal conductivities of the materials are high. Very small temperature gradients in the x-direction have previously been calculated [38] and are therefore disregarded in this work. The isothermal assumption is furthermore justified by a rough evaluation of the difference between the cell temperature and the gas temperature, presented in the appendix.

2.1 Mass Transport

The mass balance at steady state is given by

$$\nabla \vec{N}_i = r_i \qquad (7)$$

where $\vec{N}_i$ *is* the flux of species *i*, and r_i is the rate of reaction of species *i*.

2.2 Diffusion

In the dusty gas model, the molar flux of compound *i* is given as an implicit function of the other molar fluxes the molar fractions, and the gradients of pressure and molar fractions:

$$\sum_{j=1,j\neq i}^{n}\frac{X_i\vec{N}_j-X_j\vec{N}_i}{D_{ij}^{eff}}-\frac{\vec{N}_i}{D_{i,k}^{eff}}=\frac{\mathrm{p}}{RT}\nabla X_i+\frac{X_i}{RT}\left(1+\frac{Bp}{\mu_m D_{i,k}^{eff}}\right)\nabla p \quad (8)$$

where X_i is the molar fraction of species i, $D_{i,k}^{eff}$ is the effective Knudsen diffusion coefficient of species i, $D_{i,j}^{eff}$ is the effective binary diffusion coefficient of species *i* in *j*, *p* is the pressure; $\vec{N}_i$ is the flux of species *i*, *B* is the permeability and μ_{m} is the viscosity of the mixture

The binary diffusion coefficient is calculated by the Chapman–Enskog correlation and the Knudsen diffusion coefficient is calculated by kinetic theory of gases [39].

$$D_{i,j}^{eff}=\frac{\epsilon}{\tau}D_{i,j}=\frac{\epsilon}{\tau}0.001858T^{1.5}\cdot\frac{\left(\frac{1}{M_i}+\frac{1}{M_j}\right)^{0.5}}{p\sigma_{i,j}^2\Omega_D} \quad (9)$$

$$D_{i,K}^{eff}=\frac{\epsilon}{\tau}D_{i,K}=\frac{\epsilon}{\tau}\cdot\frac{d_p}{3}\sqrt{\frac{8RT}{\pi M_i}} \quad (10)$$

where M_i is the molecular weight of component *i*, $\sigma_{i,j}$ is the average collision diameter between component i and j and Ω_D is the dimensionless collision integral in the Lennard-Jones potential model, ϵ is electrode porosity, τ is the tortuosity, d_p is the pore diameter. σ and Ω_D are available in the literature [39,40]. Based on [41] where permeabilities for Ni-YSZ electrodes are summarized, we have selected a permeability of $B=5\cdot10^{-15}\ \mathrm{m}^2$.

2.3 Transport of electrons and oxygen ions

In the 2d model two charged particles are modelled, electrons and oxygen ions. The electrodes and electrolyte is assumed to be pure electronic and ionic conductors, respectively. Ohms law is used to calculate the current distribution in the 2d model.

$$\nabla(\sigma_{el}\nabla\Phi_{\mathrm{el}})=0 \quad (11)$$

$$\nabla(\sigma_{io}\nabla\Phi_{\mathrm{io}})=0 \quad (12)$$

The electronic conductivity, σ_{el}, of the electrodes is high compared to the ionic conductivity of the electrolyte, σ_{io}, and is therefore assumed to be temperature independent in the investigated temperature regime. The electronic conductivity is 800 $S\,\mathrm{cm}^{-1}$ for the cathode (Ni-8YSZ) and 72 $S\,\mathrm{cm}^{-1}$ for the anode (LSM) [42–44]. The ionic conductivity for the electrolyte is temperature dependent and given as [45]:

$$\sigma_{io}=466\cdot\exp(-\frac{9934}{T}) \quad (13)$$

where T is inserted in K and σ_{io} is in $\Omega^{-1}\mathrm{cm}^{-1}$. In the 1d model, the current density is assumed to be uniform and thus equations 11 and 12 are not used.

2.4 Reactions

Two electrochemical reactions take place at the cathode-electrolyte interface, namely the reduction of CO_2 to CO and of H_2O to H_2:

$$\mathrm{CO_2}+2\mathrm{e}^-\rightarrow\mathrm{CO}+\mathrm{O}^{2-} \quad (14)$$

$$\mathrm{H_2O}+2\mathrm{e}^-\rightarrow\mathrm{H_2}+\mathrm{O}^{2-} \quad (15)$$

The rates of reactions 14, and 15 are given as functions of the current density, see Table 1. During co-electrolysis both reaction 14 and reaction 15 may occur at the interface. In this case the current density will consist of the current arising from each of the two reactions:

$$\vec{\imath} = \vec{\imath}_{H_2O} + \vec{\imath}_{CO_2} \quad (16)$$

One approach to model co-electrolysis is to assume that only reaction 15 occurs at the interface and that subsequently CO_2 is converted to CO via the water-gas shift reaction [46]. Another approach is to assume that both reactions occur at the interface and include a parameter β, that determines the fraction of the interface surface available for H_2O electrolysis [47–49]. In this approach, the electrical current is divided between the two reactions depending on the mole fraction of CO_2 and H_2O at the interface.

$$\beta = \frac{X_{H_2O}^{int}}{X_{CO_2}^{int} + X_{H_2O}^{int}} \quad (17)$$

In this study we will use the latter method, where both reaction 14 and 15 take place at the interface.In the water-gas shift reaction occur infinite fast, the two methods should give the same. However, since the water-gas shift reaction might not reach equilibrium within the reaction zone, the latter method is used.

In the entire electrode three reactions might take place: 1) the water-gas shift reaction, 2) methanation reaction, and 3) the Boudouard reaction. Only the water-gas shift reaction is included in the model as a reaction with finite rate. The rate expression is given in Table 1. The reason for excluding the methanation reactions is that the formation of methane is severely limited by thermodynamics at the high temperature and low pressure in the electrode (calculated with in-house thermodynamics software). The carbon formation reactions are excluded because we only want to identify if carbon formation if thermodynamic feasible. It is generally accepted that carbon formation will take place when the carbon affinity a_c is above 1 [12,50]. Since SOECs are normally operated at steady state for long periods of time, any affinity for carbon is likely to cause accumulation of carbon, regardless of the reaction rate, and will eventually cause problems for the cell.

The rate expressions for reactions 14, 15 and 3 and the thermodynamic equilibrium constants for the Boudouard reaction (reaction 1) are given in Table 1.

Table 1. Reaction rates and equilibrium.

Reaction	Thermodynamic equilibrium or rate expression	Source
14	$r_{CO_2,electrolysis} = \frac{\vec{\imath}}{2F} \cdot (1-\beta) \cdot \frac{1}{d_i}$	
15	$r_{H_2O,electrolysis} = \frac{\vec{\imath}}{2F} \cdot \beta \cdot \frac{1}{d_i}$	
3	$r_{wgs} = k_{sf}\left(P_{H_2O}P_{CO} - \frac{P_{H_2}P_{CO_2}}{K_{ps}}\right)$	[38]
	$k_{sf} = 0.0171 \exp\left(-\frac{103191}{RT}\right)\ \mathrm{mol\ m^{-3}\ Pa^{-2}\ s^{-1}}$	
	$K_{ps} = \exp(-0.2935Z^3 + 0.635Z^2 + 4.1788Z + 0.3169)$	
	$Z = \frac{1000}{T} - 1$	

1 $$K_B = \exp\left(\frac{138100 - 144.6T}{RT}\right) \cdot 1\ \mathrm{atm}^{-1}$$ [13]

In Table 1 *F* is Faradays constant, p_i is the partial pressure of species *i*, *R* is the universal gas constant and, *T* is the temperature.

The reaction rate for the four species in the cathode and reaction interface can be written as:

$$r_{H_2} = r_{wgs} + r_{H_2O,electrolysis} \quad (18)$$
$$r_{H_2O} = -r_{wgs} - r_{H_2O,electrolysis} \quad (19)$$
$$r_{CO} = -r_{wgs} + r_{CO_2,electrolysis} \quad (20)$$
$$r_{CO_2} = r_{wgs} - r_{CO_2,electrolysis} \quad (21)$$

Where r_{wgs} is the reaction rate for the water-gas shift reaction. $r_{H_2O,electrolysis}$ and $r_{CO_2,electrolysis}$ are 0 in the cathode support.

In the 2d model the oxidation of the oxygen ion takes place at the anode-electrolyte interface:

$$2\,O^{-2} \rightarrow O_2 + 4e^- \quad (22)$$

$$r_{O_2} = \frac{\vec{\imath}}{4F} \quad (23)$$

The transfer of the oxygen molecules to the anode channel is calculated with the mass transfer equation (eq. 7) and the dusty gas model (eq. 8).

2.5 Boundary Conditions and Numerical Solution

It follows from the assumption of negligible mass transfer between the bulk gas in the channel and the sample, that the mole fractions of all species at the boundary between the fuel electrode and the bulk gas is identical to the bulk gas. The pressure is also the same. Thus, the boundary conditions at x = 0 for the 1d model are:

$$X_i|_{x=0} = X_{(i,channel)} \quad (24)$$
$$p|_{x=0} = p_{(t,channel)} \quad (25)$$

Where $X_{(i,channel)}$ is the mole fractions in the channel, and $p_{(t,channel)}$ is the channel pressure. $X_{(i,channel)}$ and $p_{(t,channel)}$ must be specified as input to the model.

Similar for the 2d model the boundary conditions at x=0 for the part of the cathode in contact with the cathode channel (labelled “a” on figure 2b) is given by equation 24 and 25.

Furthermore, no current is transferred from the electrode to the channel.

$$\vec{n} \cdot \vec{\imath}|_{x=0} = 0 \quad (28)$$

Where $\vec{n}$ is the normal vector to the boundary.

For the part of the cathode in contact with the interconnect (labelled “b” on figure 2b), the potential, Φ, is specified and the mass flux across the boundary is zero.:

$$\Phi|_{x=0} = 0 \quad (29)$$

$$\vec{n} \cdot \vec{N_i}|_{x=0} = 0 \quad (30)$$

The boundary conditions at the anode, x=d_c, in contact with the anode channel (labelled “j” on figure 2b) are:

$$X_i|_{x=\mathrm{d_c}} = X_{(i,channel)} \quad (31)$$

$$p|_{x=\mathrm{d_c}} = p_{(t,channel)} \quad (32)$$

$$\vec{n} \cdot \vec{\imath}|_{x=0} = 0 \quad (33)$$

For the anode in contact with the interconnect (labelled “i” on figure 2b), the current density is specified and a zero mass flux.

$$\vec{N_i} = 0 \quad (34)$$

$$\vec{\imath} = \vec{\imath}_{\mathrm{t}} \cdot \frac{w_{pitch}}{w_{rib}} \quad (35)$$

where $\vec{\imath}_{\mathrm{t}}$ is the applied current density with respect to the entire cell cross-section.

For the other boundaries in the 2d model a symmetry/insulation condition is applied:

$$\vec{n} \cdot \vec{N_i}|_{x=0} = 0 \quad (36)$$

$$\vec{n} \cdot \vec{\imath}|_{x=0} = 0 \quad (37)$$

The equations were solved in COMSOL Multiphysics (finite element method) using a damped Newton solver. The 1d model was divided into 200 elements. For the 2d model the cathode and electrode-electrolyte interface was meshed with a triangular mesh using COMSOL’s in-build “finer” mesh setting for fluid dynamics. In the electrode-electrolyte interface the mesh was refined in the x-direction by a factor of 10 and in the y-direction by a factor of 5. The electrolyte and anode were meshed with a triangular mesh using COMSOL’s in-build “extra fine” mesh setting for general physics. The actual number of elements varied with w_{pitch} and $\mathrm{d_c}$. Further refinement of the mesh (changing the in-build settings to “very fine” and “extremely fine“, respectively, showed no difference in the obtained results.

3 Results and Discussion

The result and discussion section is divided into four main parts. First the results from the 1d model are presented. Subsequently the results from the 2d model are presented and compared to the 1d model. Afterwards, the 1d model is used to investigate if diffusion limitations can explain observed carbon formation in some recent studies and, lastly, it is shown that the calculated CO mole fraction from the 2d model can be approximated by a simple linear correlation between the mole fraction in the channel and the current density. Thus makes it possible to include diffusion in current SOEC models without significant increase in calculation time.

3.1 1d model

3.1.1 Electrolysis of CO_2

Figure 3a shows the mole fraction of CO and CO_2 through the cathode layer and Figure 3b shows the corresponding equilibrium temperature for carbon formation, T_B, for a channel gas composition of 60 % CO and 40 % CO_2 and current densities of 0.4 A cm^{-2} and 0.5 A cm^{-2}, respectively. Since there is neither H_2 nor H_2O in the system, the water-gas shift reaction can be ignored. From Figure 3b it can be seen that the change in mole fraction through the cathode layer caused by the diffusion limitations, causes the equilibrium temperature to rise above the cell temperature (in this case 973 K, marked with a horizontal line in Figure 3b) and the Boudouard reaction will therefore be thermodynamically favored close to the electrode-electrolyte interface. In order to avoid the carbon formation, the temperature should either be increased by at least 10 or 20 K, for 0.4 A cm^{-2} and 0.5 A cm^{-2}, respectively or the current density must be decreased below 0.4 A cm^{-2}. With the given parameters (T, $\vec{\imath}_t$, ϵ, τ, d_e, d_p, X_{CO2}), gas diffusion limitations becomes an important phenomenon in relation to carbon formation even at moderate current densities.

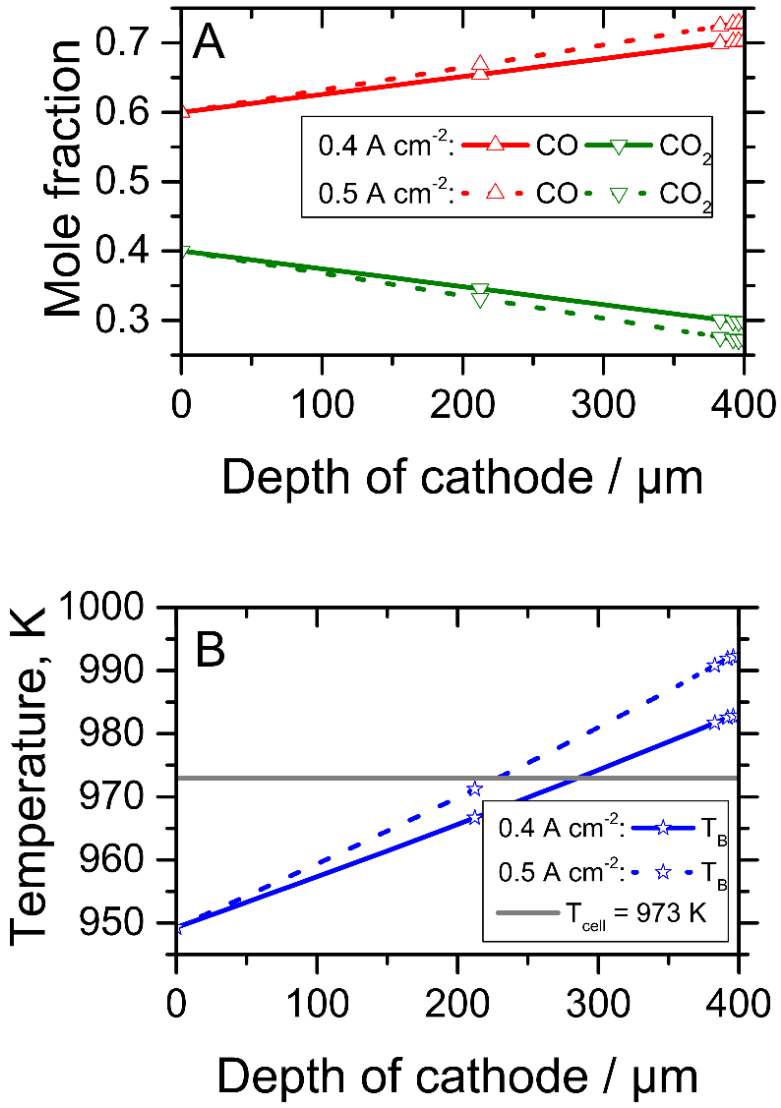

Figure 3. Mole fraction (a) and equilibrium temperature, T_B (b) profiles during CO_2 electrolysis for T=973 K, $\vec{\imath}_t$=0.4 and 0.5 A cm^{-2}, ϵ = 0.3, τ = 3, d_e = 400 µm and a CO mole fraction of 60 %. The depth of the electrode is from the gas channel, i.e. x=0 is at the gas channel and x=400 µm is at the electrode-electrolyte interface. The cell

temperature, 973 K, is marked with a gray horizontal line to clearly illustrate where the Boudouard equilibrium temperature crosses the cell temperature.

3.1.2 Electrolysis of CO_2 and H_2O (co-electrolysis)

Figure 4a shows the mole fraction of H_2 and CO (H_2O and CO_2 are omitted for clarity) through the electrode layer for $\vec{\imath}$= 0.5 and 1.0 A cm^{-2} and an overall conversion of 60 %. It is assumed that the SOEC is fed with a 40:60 mixture of H_2O and CO_2 and that the gas in the fuel channel has reached the water-gas shift equilibrium. Thus, the gas composition in the gas channel is 33% CO, 27% CO_2, 26% H_2 and 14% H_2O. The Boudouard equilibrium temperature, T_B is also shown in Figure 4b. Since the equilibrium temperature is below T_{cell} at 0.5 A cm^{-2}, but slightly above at 1.0 A cm^{-2}, carbon formation is thermodynamically unfavorable at the low current density, but favorable at the high current density. The difference in diffusion coefficients of H_2 and CO can clearly be seen in the different slopes of the CO and H_2 gradients through the electrode.

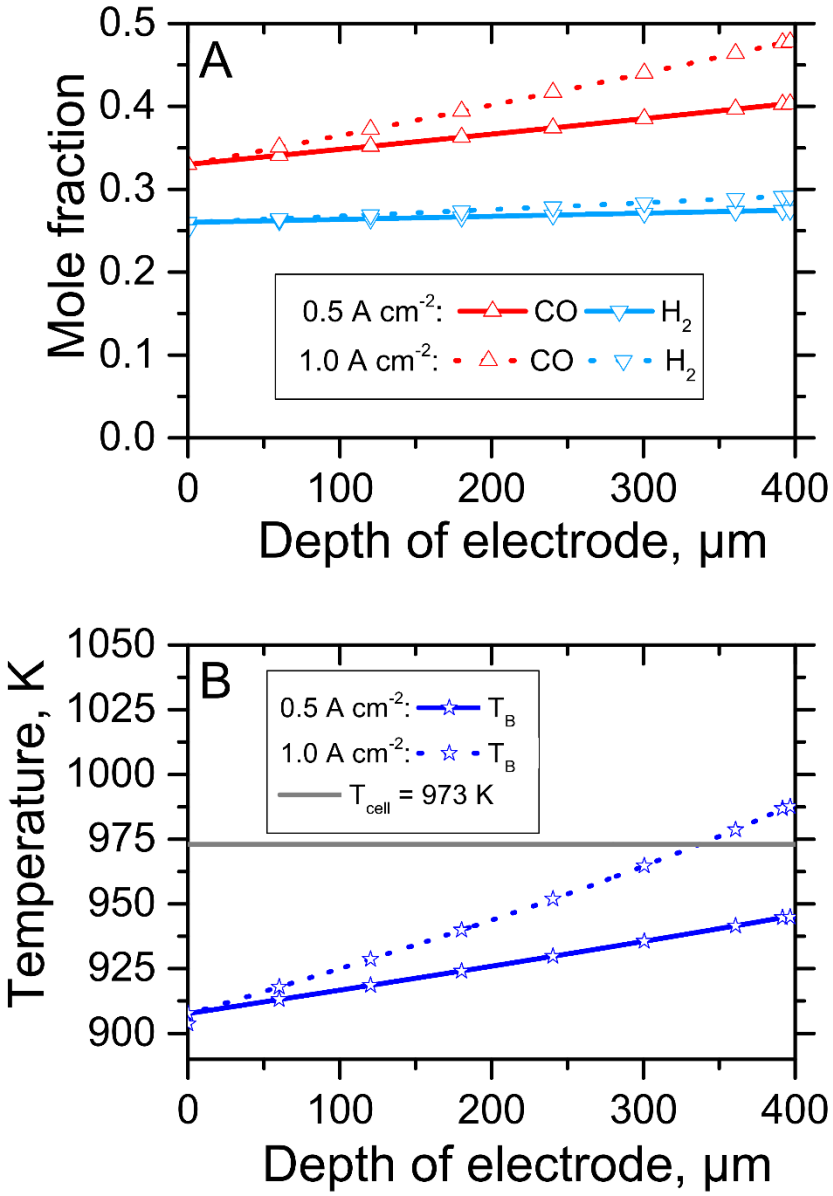

Figure 4. Mole fraction (a) and equilibrium temperature, T_B (b) profiles during co-electrolysis at T=973 K, $\vec{\imath}_t$=0.5 and 1.0 A cm^{-2}, ε = 0.3, τ = 3, de = 400 µm and an gas

channel composition of 33% CO, 27% CO_2 26% H_2 and 14% H_2O. The temperature of the cell (T_{cell} = 973 K) is marked with a gray horizontal line.

3.2 Sensitivity analysis

The parameters in the model can be divided into operating parameters (temperature, conversion and current density) and property parameters (porosity, tortuosity, electrode depth, and pore diameter). By changing only one parameter, while holding all others constant, the effect of that parameter can be investigated. In Figure 5 the effect of the parameters on the CO mole fraction at the electrode-electrolyte interface for CO_2 electrolysis is shown. All parameters, except the one being changed, were held constant at the values given in table 2

Table 2. Parameter values used for the parameter study

Parameter	Value	Unit
Current density, $\vec{i}_t$	0.75	A cm^{-2}
CO mole fraction, X_{CO}	0.5	-
Temperature, T_{cell}	1000	K
Cathode depth, d_e	400	µm
Porosity, ε	0.3	-
Tortuosity, τ	3	-
Pore diameter, d_p	0.5	µm

The results shows that 1) the effect of changing T is small, 2) changing ε/τ or d_p has a large effect when the parameter has a low value, but a low effect when they are above about 0.2 and 1 µm respectively, i.e. at about the standard values they are assigned (common values for the ε/τ fraction is 0.1 to 0.2 [29,38,51–54] and for the pore diameter it is 0.13 µm to 1.5 µm [47,51,53–55]), 3) the CO mole fraction is proportional to the CO mole fraction in the channel, current density and electrode depth. Thus, in order to minimize the CO mole fraction at the electrode-electrolyte interface, ε/τ and d_p must be above a certain value while d_e should be small. If this is not the case the CO mole fraction in the channel and the current density must be limited.

The high effect of ε/τ or d_p on the mole fraction shows that for an accurate prediction of the diffusion limitations, these parameters must be determined with good accuracy.

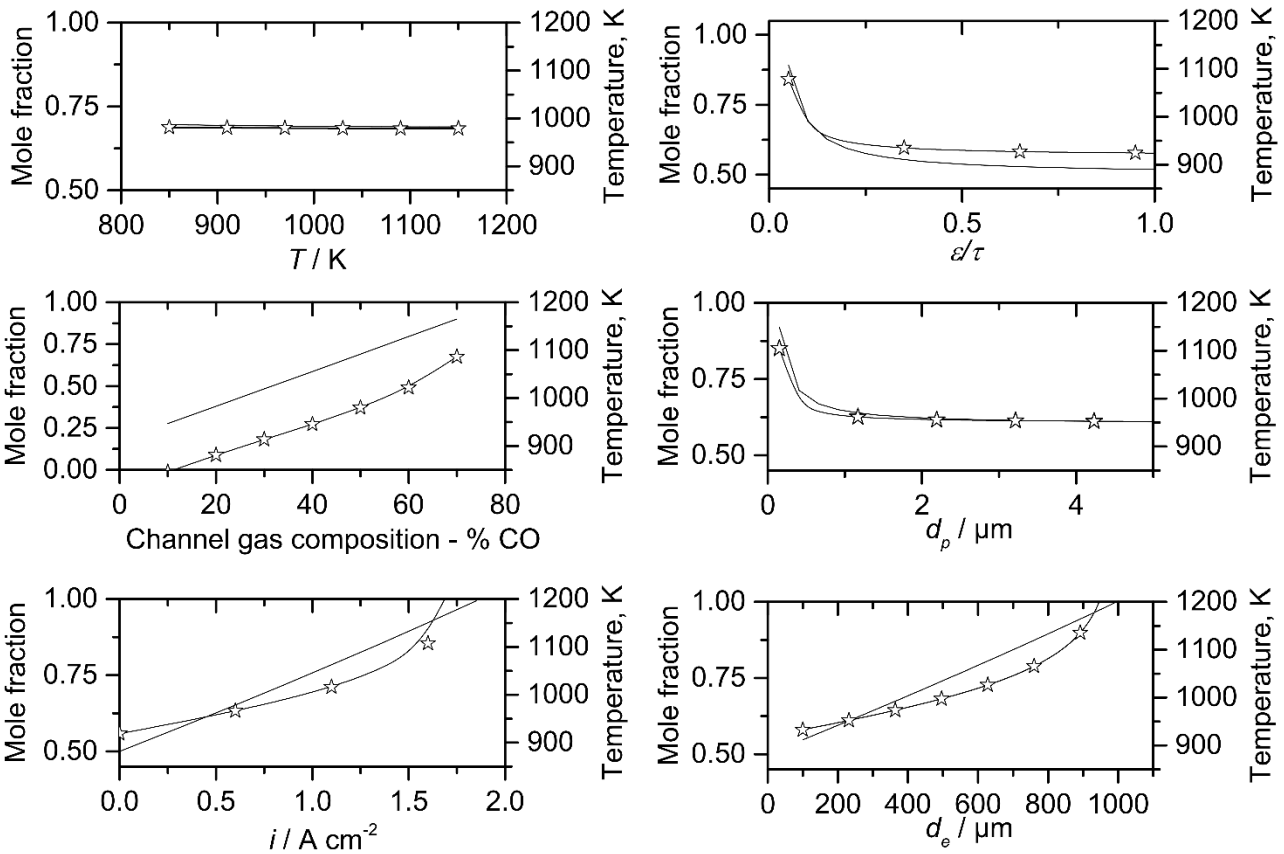

Figure 5. Effect of operating (T, X_{CO}, $\vec{i}_t$) and property (ε/τ, d_e, d_p) parameters on the mole fraction of CO (lines) and the equilibrium temperature for the Boudouard reaction, T_b, (lines with stars) at the electrode-electrolyte interface during CO_2-electrolysis. Standard conditions are listed in table 2.

3.3 2d model

3.3.1 Electrolysis of CO2

Figure 6 shows the mole fraction of CO for a case with w_{pitch} = 1 mm and w_{rib} = 0.5 mm (similar conditions as used in section 3.1.1. for the 1d model). At point “me” the CO mole fraction is 0.75 at the electrode-electrolyte interface, which is close to the 1d model (where it is 0.72, see figure 3). Moving to the right, the CO mole fraction increase, especially under the rib (from z=0.5 mm) and reaches a mole fraction of 0.89 at point “de”. This increase corresponds to an increase in the Boudouard equilibrium temperature from 1000 K to 1071 K. This is a large increase compared to the 995 K calculated with the 1d model and shows the importance of including the effect of the rib on gas transfer. The increase in Boudouard equilibrium temperature means that the temperature of the cell must be increased above 1071 K in order to thermodynamically suppress the formation of carbon.

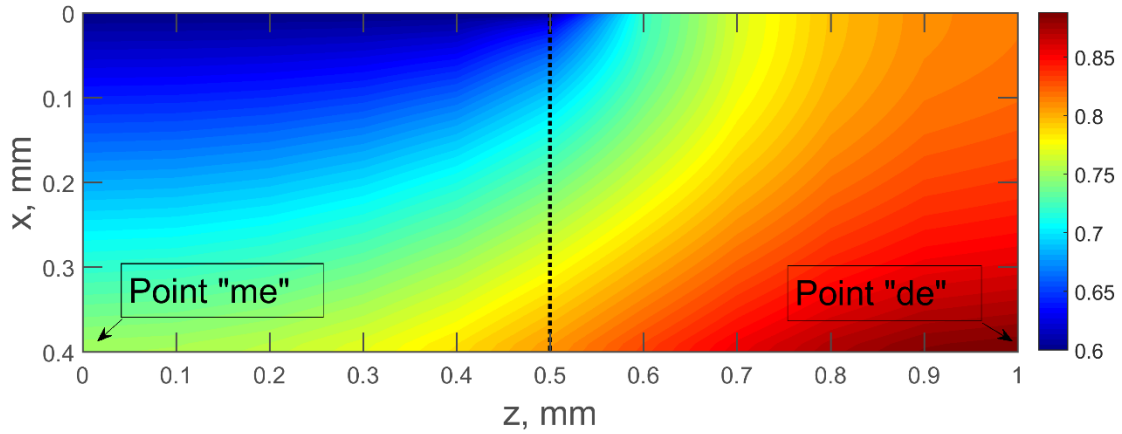

Figure 6. CO mole fraction in the cathode and reaction interface layers. The vertical line at z= w_{rib} = 0.5 mm separates the domain under the channel (left of the vertical line) and the domain under the rib (right of the line). Conditions: T=973 K, $\vec{\imath}_t$=0.5 A cm^{-2}, ϵ = 0.3, τ = 3, d_e = 400 µm X_{CO} = 0.6, w_{pitch} = 1 mm and w_{rib} = 0.5 mm.

3.3.2 Electrolysis of CO_2 and H_2O (co-electrolysis)

Figure 7 shows the mole fraction and Boudouard equilibrium temperature for a case with w_{pitch} = 1 mm and w_{rib} = 0.5 mm with a gas channel composition of 33% CO, 27% CO_2 26% H_2 and 14% H_2O at 0.5 A cm^{-2} (similar to figure 4). At point "me" the CO mole fraction is 0.425, which is slightly above the 0.40 obtained with the 1d model (see figure 4). At the right side the CO mole fraction increases to 0.52 at point "de". This corresponds to an increase in the Boudouard equilibrium temperature from 947 K to 988 K. In the 1d model the equilibrium temperature is calculated to be 970 K.

The reason for the lower Boudouard equilibrium temperature for the 2d model at point "me" is that the absolute pressure is lower than in the 1d model (not shown).

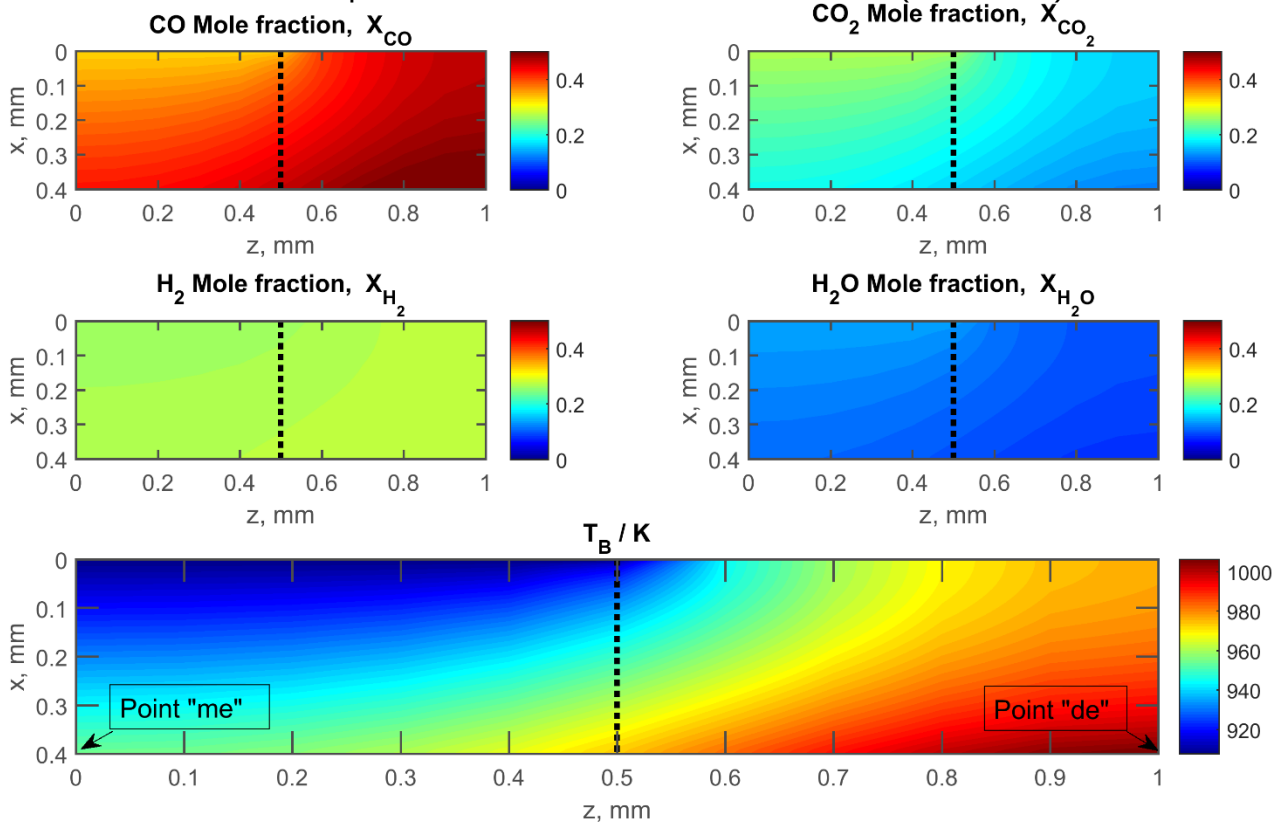

Figure 7. Mole fraction and Boudouard equilibrium temperature in the cathode and reaction interface layers. The vertical line at z= w_{rib} = 0.5 mm separates the domain under the channel (left of the line) and the domain under the rib (right of the line). Conditions: T=973 K, $\vec{\imath}_t$=0.5, ε = 0.3, τ = 3, d_e = 400 µm, gas composition: 33% CO, 27% CO_2 26% H_2 and 14% H_2O, w_{pitch} = 1 mm and w_{rib} = 0.5 mm.

3.3.3 Effect of w_{pitch} and w_{rib}.

The effect of w_{pitch} and w_{rib} is illustrated on Figure 8 for electrolysis of CO_2 in terms the difference between the CO concentration under the rib and under the channel. From the figure it can be seen that the difference between the mole fraction beneath the rib (point "de") and the mole fraction beneath the channel (point "me") increase as w_{pitch} and w_{rib} are increased. Especially an increase of the mole fraction difference is observed when w_{rib} is increased.

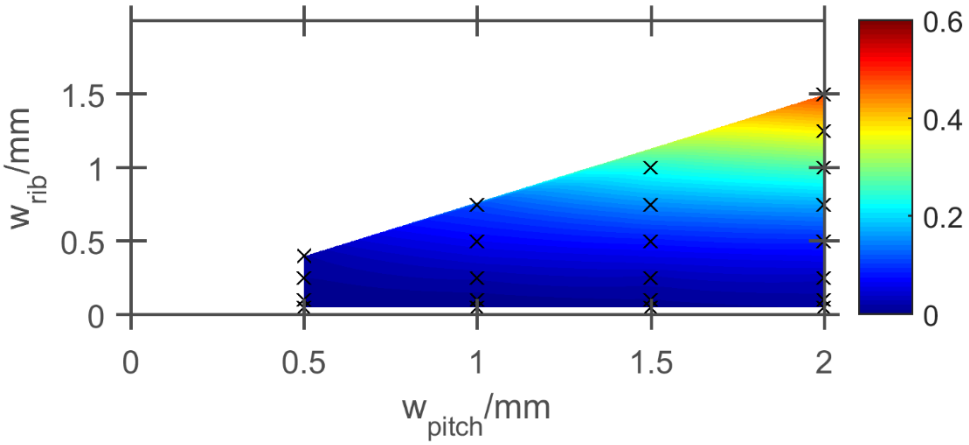

Figure 8: Difference in CO concentration (as mole fraction) between point "de" and "me" at different combinations of w_{pitch} and w_{rib}. The surface is linear interpolated based on the data points marked with black x's. T = 1000 K, ε =0.3, τ =3, d_e = 400 µm, d_p = 0.5 µm, $\vec{\imath}_t$ = 0.25 A cm^{-2}, X_{CO} = 0.25

3.4 Comparison with Literature

During an experimental study of carbon formation in CO_2-electrolysis, Skafte et al. [2] found that carbon was formed at CO/CO_2 ratios in the gas channel thermodynamically unfavorable for the reaction. In one case, carbon was observed at 1023 K with a current density of 0.39 A cm^{-2} and an outlet mole fraction of 73 % CO (calculated from the article). The size of the cell was 53 mm by 53 mm with an active area of 40 mm by 40 mm. We have assumed that the current density and flow is uniform across the cell, and thus modelled the diffusion with the 1d model (ignoring the effect of ribs from interconnects). The physical properties of the cell are not given; however, assuming an electrode thickness of 310 µm, a porosity of 30 % and a tortuosity of 3 (based on data on similar cells used by the same authors) the equilibrium temperature for the Boudouard reaction is calculated to be 5 K above the actual temperature. This indicates that diffusion limitations in the electrode can explain why carbon was formed in their study.

In a recent study by Tao et al. [6] carbon formation was observed during co-electrolysis at 67 % conversion, where the formation should be thermodynamically unfavored up to above 99 % conversion. A total of five cells with different current densities and porosities were tested (Table 3). The electrode thickness was ~315 µm, the tortuosity was around 3

(based on the model fitting in the article) and the temperature was 1123 K at open circuit voltage and increased to 1148 K at current densities of 2.0 A cm^{-2}. The size of the cells was 50 mm by 50 mm with an active area of 40 mm by 40 mm.

For cell 4 and 5 carbon formation was observed, while no carbon was observed for cell 1-3. From impedance spectroscopy an increase in both the conversion impedance and diffusion impedance was observed for cell 4 and 5. Furthermore the porosity was lower in cells 4 and 5. An increase in conversion impedance means a higher mole fraction of either $CO+H_2$ or CO_2+H_2O. The increase in diffusion impedance is caused by a change between the bulk gas and the gas composition at the interface. Based on this, the authors suggest that the carbon formation is caused by diffusion limitations. This is also in agreement with figure 5, where it can be seen that a change in porosity can cause a significant increase in the product mole fraction at the interface due to diffusion limitations.

Table 3. Properties of the five cells tested by Tao et al. [1]

Cell	Current density $\vec{\imath}_t$ / A cm^{-2}	Gas conversion γ / %	Estimated porosity / %	Carbon observed
1	1.5	45	30-40	No
2	2.0	59	30-40	No
3	2.0	59	30-40	No
4	2.0	59	20	Yes
5	2.25	67	25	Yes

The hypothesis that diffusion limitations caused the carbon formation was tested with the 1d diffusion model. Again, we have assumed that the flow and current is distributed uniformly across the cell and have thus used the 1d model (ignoring the effect of ribs from interconnects). This was selected due to the small dimensions of the cell. Furthermore, if the 1d model predicts risk of carbon formation, the 2d model would certainly also predict risk of carbon formation. The gas channel composition was computed by bringing the gas to the water-gas shift equilibrium. Figure 9 shows the equilibrium temperature for the Boudouard reaction as a function of current density and porosity at the electrode-electrolyte interface.

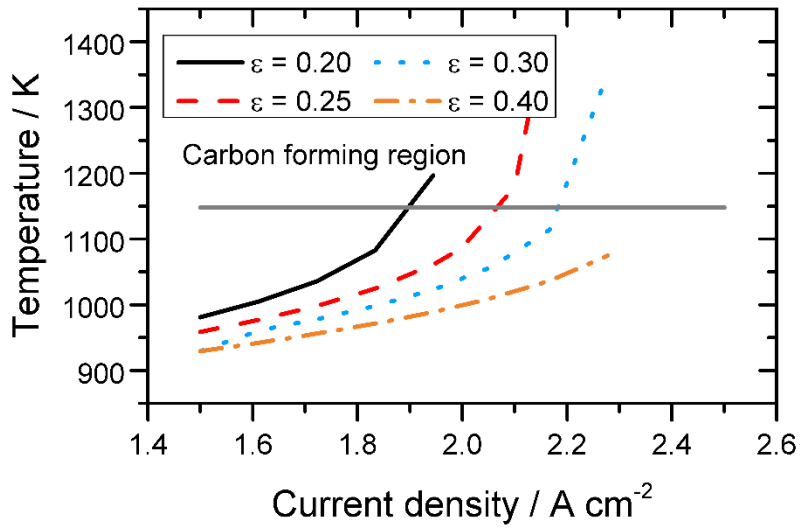

Figure 9. Equilibrium temperature for the Boudouard reaction at the electrode-electrolyte interface as function of the current density at different levels of porosity. The horizontal line is the temperature of the cell (1148 K) in the test in [[1]**].**

Conditions: T=1148 K, ε = 0.3, d_e = 315 µm. The gas composition was 0.45(1-γ) H_2O, 0.45(1-γ) CO_2, 0.10+0.45(γ) H_2, 0.45(γ) CO, where the conversion γ is a function of $\vec{\imath}_t$ and interpolated from table 3.

Since the porosity for cell 1-3 was 30-40 %, it can be seen from the blue and yellow curve in figure 9 that T_B for these cells lie below the temperature of cell at i = 1.5 to 2.0 A cm^{-2} (the reaction is thermodynamically unfavored). However, for cell 4 with a porosity of 20 %, it can be seen that the corresponding black line in Figure 9 crosses T_{cell} at a current density of 1.9 A cm^{-2} i.e. below 2.0 A cm^{-2} used in the experiment. Similarly, for cell 5, the red line shows that T_B crosses T_{cell} at a current density below 2.5 A cm^{-2}, thus suggesting that carbon formation locally in the cell is thermodynamically favorable. The diffusion limitations thus seem to explain the observed carbon formation in cells 4 and 5.

3.5 Implementation of the rib effect in existing models

Several existing models of SOEC only calculate the gas composition in the gas channel [56,57] or neglect the effect of the ribs on the gas concentration within the electrode [38,42,51,58]. For such models it would be advantageous if the gas composition under the rib could be found directly from the gas composition within the gas channel and operational parameters ($\vec{\imath}$, T), since this will not significantly increase the computational time. When the gas composition has been calculated, the carbon affinity can be calculated and the risk of carbon formation can be assessed.

For large 3d models of entire stacks, the difference in scale of the involved structures (e.g. mm to cm for inlet manifolds and interconnect channels and µm for the electrode) makes the detailed modelling of the diffusion under the interconnect ribs infeasible. Homogenization techniques are already used in some models to reduce the number of degrees of freedom from billions to tens of thousands [59], so including a detailed modelling of the diffusion in the electrode in each cell in the stack would be undesirable. To investigate if the gas composition beneath the rib could be expressed as a simple function of gas composition in the channel and the operational parameters, we used the 2d model to calculate the gas composition with the parameters given in Table 4. The parameters describing the microstructure and the interconnect structure were fixed. Those parameters will not vary significantly across the cell and from cell-to-cell. The temperature influence is omitted due to the small influence observed in Figure 5.

Table 4. Parameter values used for figure 10

Parameter	Value	Unit
Current density, $\vec{\imath}_t$	0.1, 0.25, 0.5, 0.75	A cm^{-2}
CO mole fraction, X_{CO}	0.13, 0.25, 0.46, 0.63	-
Temperature, T_{cell}	1023	K
Pitch width, w_{pitch}	1	mm
Rib width, w_{rib}	0.5	mm
Cathode depth, d_e	400	µm
Porosity, ε	0.3	-
Tortuosity, τ	3	-
Pore diameter	0.5	µm

Figure 10 shows the difference between the CO mole fraction in the gas channel and point “me” (beneath the center of the channel) and point “de” (beneath the center of the rib), respectively. The difference between the CO mole fraction in the channel and the average CO mole fraction at the boundary labelled “e” in figure 2b is also shown. The average mole

fraction is calculated using elementwise integration with numeric quadrature of 4th order (standard in COMSOL).

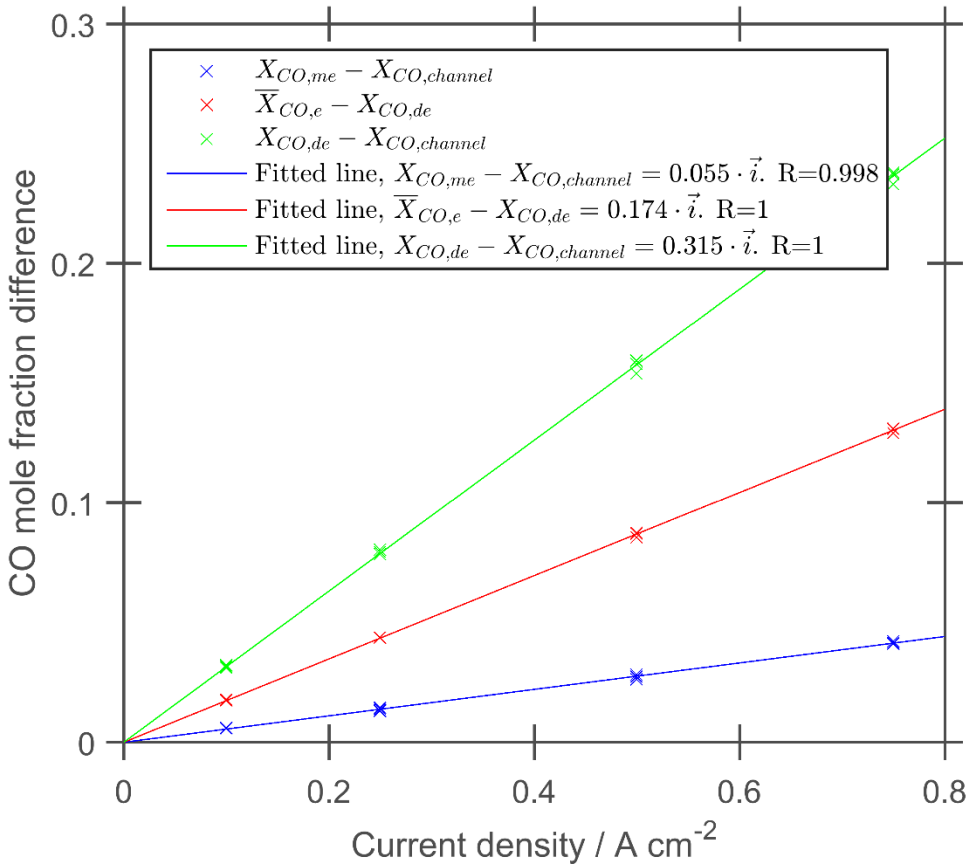

Figure 10 CO mole fractions difference between the channel and the point beneath the middle of the channel (point "me"), the point beneath the middle of the rib (point "de"), and the average mole fraction on boundary "e". Conditions are given in table 4.

The figure shows that the CO mole fraction at the points and at the boundary "e" can be calculated directly from the current density and the CO mole fraction in the channel:

$$X_{CO}|_{point\ me} - X_{CO}|_{channel} = 0.055 \cdot \vec{i}_t \quad (38)$$

$$\overline{X_{CO}}|_{boundary\ e} - X_{CO}|_{channel} = 0.174 \cdot \vec{i}_t \quad (39)$$

$$X_{CO}|_{point\ de} - X_{CO}|_{channel} = 0.315 \cdot \vec{i}_t \quad (40)$$

The function will change when the parameters relating to the cell (ε, τ, d_e, d_p, w_{pitch}, w_{rib}) are changed, or if the temperature is changed significantly. However, it is relatively simple to calculate a new correlation based on a 2d simulation with new parameters.

The credibility of the perfect linear fits can be investigated by examine the dusty gas model. For a binary gas mixture (CO-CO_2 as present in Figure 10) equation (8) reduces to:

$$\frac{X_{CO}\vec{N}_{CO_2}-X_{CO_2}\vec{N}_{CO}}{D^{eff}_{CO-CO_2}}-\frac{\vec{N}_{CO}}{D^{eff}_{CO,k}}=\frac{\mathrm{p}}{RT}\nabla X_{CO}+\frac{X_{CO}}{RT}\left(1+\frac{Bp}{\mu_m D^{eff}_{CO,k}}\right)\nabla p \qquad (41)$$

Using Graham's law, $\vec{N}_{CO_2}/\vec{N}_{CO}=\sqrt{(M_{CO}/M_{CO_2})}$ and the relationship between the mole fractions, $X_{CO_2}=1-X_{CO}$, equation (41) reduces further to:

$$-\vec{N}_{CO}\left(\frac{1-bX_{CO}}{D^{eff}_{CO-CO_2}}+\frac{1}{D^{eff}_{CO,k}}\right)=\frac{\mathrm{p}}{RT}\nabla X_{CO}+\frac{X_{CO}}{RT}\left(1+\frac{Bp}{\mu_m D^{eff}_{CO,k}}\right)\nabla p \qquad (42)$$

where $b=1-\sqrt{(M_{CO}/M_{CO_2})}$

Assuming that diffusion only take place in the x direction, approximating ∇X_{CO} by $\Delta \mathrm{X_{CO}}/\Delta x$ and rearranging leads to:

$$\Delta X_{CO}=\left(-\vec{N}_{CO}\left(\frac{1-bX_{CO}}{D^{eff}_{CO-CO_2}}+\frac{1}{D^{eff}_{CO,k}}\right)-\frac{X_{CO}}{RT}\left(1+\frac{Bp}{\mu_m D^{eff}_{CO,k}}\right)\nabla p\right)\cdot\frac{\mathrm{RT}}{\mathrm{p}}\Delta \mathrm{x} \qquad (43)$$

The pressure difference can be calculation with [9]:

$$\nabla p=\frac{-RT\sum_i^n\frac{N_i}{D^{eff}_{i,k}}}{1+\sum_i^n\frac{X_i Bp}{\mu_m D^{eff}_{i,k}}}=\frac{-RT\vec{N}_{CO}\left(\frac{1}{D^{eff}_{CO,k}}+\frac{\sqrt{M_{CO}/M_{CO_2}}}{D^{eff}_{CO_2,k}}\right)}{1+\frac{X_{CO}Bp}{\mu_m D^{eff}_{CO,k}}+\frac{(1-X_{CO})Bp}{\mu_m D^{eff}_{CO_2,k}}} \qquad (44)$$

Equation (43) can thus be rewritten to

$$\Delta X_{CO}=\left(-\vec{N}_{CO}C_1-\vec{N}_{CO}X_{CO}\mathrm{C_2}\right)\cdot\Delta \mathrm{x} \qquad (45)$$

where:

$$\mathrm{C_1}=\left(\frac{1-bX_{CO}}{D^{eff}_{CO-CO_2}}+\frac{1}{D^{eff}_{CO,k}}\right)\cdot\frac{\mathrm{RT}}{\mathrm{p}} \qquad (46)$$

$$\mathrm{C_2}=\left(1+\frac{Bp}{\mu_m D^{eff}_{CO,k}}\right)\frac{-\left(\frac{1}{D^{eff}_{CO,k}}+\frac{\sqrt{M_{CO}/M_{CO_2}}}{D^{eff}_{CO_2,k}}\right)}{1+\frac{X_{CO}Bp}{\mu_m D^{eff}_{CO,k}}+\frac{(1-X_{CO})Bp}{\mu_m D^{eff}_{CO_2,k}}}\cdot\frac{\mathrm{RT}}{\mathrm{p}} \qquad (47)$$

Since b is low ($1-\sqrt{(M_{CO}/M_{CO_2})}=0.2$) and $D^{eff}_{CO-CO_2}$ and $D^{eff}_{CO,k}$ are the same order of magnitude at the operation conditions, $\mathrm{C_1}$ will not vary much when X_{CO} is varied. Also, since $D^{eff}_{CO,k}$ and $D^{eff}_{CO_2,k}$ are at the same order of magnitude, the denominator of $\mathrm{C_2}$, and consequently $\mathrm{C_2}$, will not vary much with changes in X_{CO}. Indeed, calculating and comparing the two constant at $X_{CO}=0$ and $X_{CO}=1$ showed only a difference of 6 % compared to values calculated at $X_{CO}=0.5$.

From Figure 3 it can be seen that the mole fraction decrease linear from the channel to the reaction zone. Thus, it is reasonable to fix X_{CO} as:

$$X_{CO}=\frac{X_{CO}|_c+(X_{CO}|_c+\Delta X_{CO})}{2}=\frac{X_{CO}|_c}{2}+\frac{X_{CO}|_c}{2}+\frac{\Delta X_{CO}}{2} \qquad (47)$$

Inserting into equation 45 and rearranging yields:

$$\Delta X_{CO} + \frac{\Delta X_{CO}}{2}\vec{N}_{CO}C_2\Delta x = \left(-\vec{N}_{CO}C_1 - \vec{N}_{CO}X_{CO}|_c\mathrm{C}_2\right)\cdot \Delta\mathrm{x} \quad (48)$$

$$\Delta X_{CO} = \frac{\left(-\vec{N}_{CO}C_1 - \vec{N}_{CO}X_{CO}|_c\mathrm{C}_2\right)\cdot\Delta\mathrm{x}}{1+0.5\vec{N}_{CO}C_2\Delta x} \quad (49)$$

Since the diffusion flux, $\vec{N}_{CO}$, and distance, Δx, are rather small in this study, the term $0.5\vec{N}_{CO}C_2\Delta\mathrm{x}$ in the denominator of equation (49) will be of the order of magnitude 10^{-2}. This means that the mole fraction difference can be expresses as in equation (50) and since $\vec{N}_{CO}$ is directly proportional to the current distribution, the linear relationship observed in Figure 10 is reasonable.

$$\Delta X_{CO} \approx -\vec{N}_{CO}(C_1 + X_{CO}|_c\mathrm{C}_2)\cdot\Delta\mathrm{x} \quad (50)$$

4. Conclusion

In this work, two models for diffusion from the gas channel through the electrode layer towards the reaction interface of a solid oxide electrolysis cell have been set up and solved using COMSOL Multiphysics. The simulations showed that carbon formation may be an operational risk due to diffusion limitations that influence the reactant mole fractions in the electrode material. The risk may be severe for CO_2-electrolysis, but is also significant for co-electrolysis.

When the ε/τ ratio is less than 0.3 or the pore diameter, $d_{p,}$ is less than 1 µm, the concentration gradient of CO from the channel to the interface becomes large and care must be taken in selecting an appropriately conservative (low) current density and gas conversion or a high operating temperature to avoid carbon formation. When including the effect of the rib from the interconnect, it is clear that the rib causes an increase in the CO mole fraction even at low widths. The effect of the rib on the CO concentration at the electrode-electrolyte interface can be approximated by a simple linear function of the current density and channel gas composition for CO_2-electrolysis. This function needs to be updated if the parameters relating to the cell (ε, τ, d_e, $d_{p,}$ w_{pitch}, w_{rib}) are changed. However, once that is done, it allows for an easy and low computational cost inclusion to existing cell and stack models. The perfect observed linear fit was justified by examine the dusty gas model.

Simulation of two cases from the literature, where carbon formation was observed, showed that the observed carbon formation can be explained by diffusion limitations.

The results show clearly that diffusion limitations on transport of reactants and products in electrolyzer cells may lead to significant concentration gradients inside the electrode material. This in turn may create conditions favorable for the formation of carbon even under operating conditions where carbon formation would not otherwise be expected to occur based solely on the channel gas composition. Our work shows that models accounting for both reaction and diffusion inside SOEC electrodes are needed - both at the design stage and during operation - as means to avert potentially devastating carbon formation.

Acknowledgements

This project is a collaboration between the CHEC Research center at DTU Chemical Engineering and Haldor Topsoe A/S and is partially funded by the Danish Industrial Ph.D. Fellowship Programme administered by Innovation Fund Denmark.

List of Symbols

a_c	Carbon affinity
c	Fitting parameter
c_p	Heat capacity / J mol^{-1} K^{-1}
C_1	Diffusion term used in equation (45)
C_2	Pressure difference term used in equation (45)
d	Fitting parameter
d_{anode}	Depth of anode / µm
d_c	Cell depth / µm
d_e	Depth of cathode / µm
$d_{\text{electrolyte}}$	Depth of electrolyte / µm
d_p	Pore diameter / µm
$D_{\text{i,k}}^{\text{eff}}$	Effective Knudsen diffusion coefficient of species i / m^2 s^{-1}
$D_{\text{i,j}}^{\text{eff}}$	Effective binary diffusion coefficient of species i and j / m^2 s^{-1}
E_{act}	Activation energy / kJ mol^{-1}
F	Faradays constant / 96485 C mol^{-1}
ΔH	Reaction enthalpy / J mol^{-1}
$\vec{\imath}$	Current density flux / A cm^2
$\overrightarrow{\imath_t}$	Applied current density at the boundary / A cm^2
K_1	Equilibrium constant / atm^{-1}
k	Thermal conductivity / W m^{-1} K^{-1}
M	Molar mass / g m^{-3}
m	Fitting parameter
$\overrightarrow{N_i}$	Molar flux of species i/ mol m^{-2} s^{-1}
n_e	Number of electrons
p	Pressure / atm
R	Universal gas constant / 8.31445 J mol^{-1} K^{-1}
r	Reaction rate / mol m^{-3} s^{-1}
T	Temperature / K
T_B	Equilibrium temperature for the Boudouard reaction / K
U_{cell}	Cell voltage / V
Q_{eq}	Reaction quotient / atm^{-1}
Q	Heat source / W m^{-3}
q_0	Heat convection / W m^{-2}
X_i	Mole fraction of species i
w_{pitch}	Halfwidth of the pitch / mm
w_{rib}	Halfwidth of the rib / mm
α	Charge transfer coefficient
β	Ratio of gas species at reaction interface
ε	Porosity
η	Ovenpotential / V

σ	Average collision diameter / m
σ_{el}	Electrical conductivity / $S\ \mathrm{cm}^{-1}$
σ_{io}	Ionic conductivity / $S\ \mathrm{cm}^{-1}$
γ	Pre-factor / A m^{-2}
ρ	Density / g cm^{-3}
τ	Tortuosity
μ	Viscosity / Pa s
Ω	Dimensionless collision integral
Φ	Potential / V

4 Appendix

4.1 Evaluation of validity of isothermal assumption

In order to validate the assumption of isothermal conditions, the modelling domain of the 1d model was extended to include the electrolyte and anode, and the governing energy equation was added.

The steady state governing equation for the energy is given by:

$$0 = -k_{eff}\nabla^2 \cdot T + Q \quad (51)$$

Where k_{eff} is the effective conduction, Q is the heat source. k_{eff} is calculated from the conduction of the fluid and solid in the porous media:

$$k_{eff} = \epsilon k_{fluid} + (1-\epsilon)k_{solid} \quad (52)$$

For the electrolyte, the effective conduction coefficient reduces to $k_{eff} = k_{solid}$.

The heat source Q, is calculated from the reaction heat from the electrochemical reactions (16 and 17), the water-gas shift reaction and the Joule heating:

$$Q = Q_{H_2O} + Q_{CO_2} + Q_{WGS} + Q_J \quad (53)$$

$$Q = \left(\frac{\beta}{2F}\Delta H_{H_2O} + \frac{(1-\beta)}{2F}\Delta H_{CO_2} + U_{cell}\right) \cdot \frac{\vec{\imath}}{d_i} + \Delta H_{WGS} R_{wgs} \quad (54)$$

Where ΔH_i is the reaction enthalpy for the reaction (calculated from [60]) and U_{cell} is the cell voltage calculated as:

$$U_{cell} = E + \eta_{act}^{anode} + \eta_{act}^{cathode} + \eta_{ohmic} \quad (55)$$

Where E is the equilibrium potential (including concentration overpotential) and is expressed from the Nernst's equation [51]:

$$E = E_{CO_2} = 1.46713 - 0.0004527 \cdot T + \frac{RT}{2F}\ln\left(\frac{p_{CO}(p_{O_2})^{0.5}}{p_{CO_2}}\right) \quad (56)$$

η_{act}^{anode} and $\eta_{act}^{cathode}$ are the activation potentials calculated with the Butler-Volmer equation and using a power law to calculate the exchange current densities [61]:

$$i = i_{0,anode}\left(\exp\left(\frac{\alpha_{anode}\, n_e F \eta_{act}^{anode}}{RT}\right) - \exp\left(\frac{-(1-\alpha_{anode}) n_e F \eta_{act}^{anode}}{RT}\right)\right) \quad (57)$$

$$i = i_{0,cathode}\left(\exp\left(\frac{\alpha_{cathode}\, n_e F \eta_{act}^{cathode}}{RT}\right) - \exp\left(\frac{-(1-\alpha_{cathode}) n_e F \eta_{act}^{cathode}}{RT}\right)\right) \quad (58)$$

$$i_{0,anode} = \gamma_{anode}\left(p_{O_2,anode}\right)^m \exp\left(\frac{-E_{act,anode}}{RT}\right) \quad (59)$$

$$i_{0,anode} = \gamma_{cathode}\left(p_{CO_{cathode}}\right)^c \left(p_{CO_2,cathode}\right)^d \exp\left(\frac{-E_{act,cathode}}{RT}\right) \quad (60)$$

η_{ohmic} is the ohmic loss due to resistance:

$$\eta_{ohmic} = R_{ohm} i \quad (61)$$

$$R_{ohm} = \frac{d_{anode}}{\sigma_{anode}} + \frac{d_{electrolyte}}{\sigma_{electrolyte}} + \frac{d_{cathode}}{\sigma_{cathode}} \quad (62)$$

Where d is the thickness of the layers and σ is the electrical conductivity. The electrical conductivity is given in section 2.3.

All the heat sources, except the reaction enthalpy for the water-gas shit reaction, are placed in the electrolyte [62].

As a boundary condition, the heat convection to the channels are calculated using a Nusselt number of 3.68 [62] and assuming a rectangular channel with a width of 2 mm and a height of 1 mm:

$$\frac{\partial k_{\text{eff}}\, T|_{x=0}}{\partial x} = \frac{Nu \cdot k_{fluid}}{D_H} \cdot \left(T - T_g\right) \quad (63)$$

$$\frac{\partial k_{\text{eff}}\, T|_{x=\text{d}_{\text{cell}}}}{\partial x} = \frac{Nu \cdot k_{fluid}}{D_H} \cdot \left(T - T_g\right) \quad (64)$$

At both gas channels the gas temperature, T_g, is 1023 K. In the cathode channel the properties of CO_2 is used and in the anode channel the properties air is used. Heat transfer via radiation is neglected.

Table 5 list the parameters used and table 6 shows the maximum temperature deviation between the solid part of the cell and the channel. From table 6 it can be seen that the temperature difference is within ±2 K. Since figure 5 showed that small temperature differences does not influence the diffusion, the isothermal assumption is fair to make.

Table 5. Parameter values

Parameter	Value	Unit	Source
Temperature, T	1023	K	
Pitch width, w_{pitch}	1	mm	
Rib width, w_{rib}	0.5	mm	
Cathode depth, d_e	400	µm	
Porosity, ε	0.3	-	
Tortuorosity, τ	3	-	
Pore diameter	0.5	µm	
Thickness anode, d_{anode}	15	µm	
Thickness electrolyte, $d_{electrolyte}$	15	µm	
Thermal conductivity, cathode	7.5	W m^{-1} K^{-1}	[63]
Thermal conductivity, electrolyte	2.3	W m^{-1} K^{-1}	[64]
Thermal conductivity, anode	0.8	W m^{-1} K^{-1}	[63]
Thermal conductivity, CO_2	0.066	W m^{-1} K^{-1}	[65]
Thermal conductivity, air*	0.070	W m^{-1} K^{-1}	[65]
Density, cathode	5.5	g cm^{-3}	[63]
Density, electrolyte	5.8	g cm^{-3}	[64]

Density, cathode	6.5	g cm^{-3}	[66]
Pre-factor anode, γ_{anode}	$1.52 \cdot 10^8 T$	A m^{-2}	[61]
Pre-factor cathode, $\gamma_{cathode}$	$4.56 \cdot 10^6 T$	A m^{-2}	[61]
Activation energy anode, $E_{act,anode}$	139.86	kJ mol^{-1}	[61]
Activation energy cathode, $E_{act,cathode}$	118.64	kJ mol^{-1}	[61]
Charge transfer coefficient anode, α_{anode}	0.65	-	[61]
Charge transfer coefficient cathode, $\alpha_{cathode}$	0.62	-	[61]
Fitting parameter, *c*	-0.058	-	[61]
Fitting parameter, *d*	0.25	-	[61]
Fitting parameter, *m*	0.22	-	[61]

*Calculated as 79 % N_2 and 21 % O_2

Table 6. Temperature difference at various current densities.

Current density, A cm^{-2}	Maximum temperature difference, K	
	CO_2-electrolysis. Channel composition: 50 % CO, 50 % CO_2	CO-electrolysis. Channel composition: 33% CO, 27% CO_2 26% H_2 and 14% H_2O
0.25	-1.7	-1.5
0.5	-1.8	-1.5
0.75	-0.8	-0.2
1	+1.2	+2.0

References

[1] Y. Tao, S. D. Ebbesen, M. B. Mogensen, *J. Electrochem. Soc.* **2014**, *161*, 3.
[2] T. L. Skafte, C. Graves, P. Blennow, J. Hjelm, *ECS Trans.* **2015**, *68*, 1.
[3] J.-W. Snoeck, G. F. Froment, M. Fowles, *Ind. Eng. Chem. Res.* **2002**, *41*, 17.
[4] H. He, J. M. Hill, *Appl. Catal. A Gen.* **2007**, *317*, 2.
[5] Y. Kim, J. H. Kim, J. Bae, C. W. Yoon, S. W. Nam, *J. Phys. Chem. C* **2012**, *116*, 24.
[6] Y. Tao, S. D. Ebbesen, M. B. Mogensen, *J. Electrochem. Soc.* **2014**, *161*, 3.
[7] J. Yuan, B. Sundén, *Int. J. Heat Mass Transf.* **2014**, *69*.
[8] Y. Vural, L. Ma, D. B. Ingham, M. Pourkashanian, *J. Power Sources* **2010**, *195*, 15.
[9] A. Bertei, C. Nicolella, *J. Power Sources* **2015**, *279*.
[10] R. Suwanwarangkul, E. Croiset, M. W. Fowler, P. L. Douglas, E. Entchev, M. A. Douglas, *J. Power Sources* **2003**, *122*, 1.
[11] S. Wang, W. M. Worek, W. J. Minkowycz, *Int. J. Heat Mass Transf.* **2012**, *55*, 15–16.
[12] S. Helveg, J. Sehested, J. R. Rostrup-Nielsen, *Catal. Today* **2011**, *178*, 1.
[13] J. R. Rostrup-Nielsen, *J. Catal.* **1972**, *27*, 3.
[14] P. K. D. Bokx, A. J. H. M. Kock, E. Bolellard, W. Klop, J. W. Geus, *J. Catal.* **1985**, *96*, 2.
[15] A. J. H. M. Kock, P. K. D. Bokx, E. Bolellard, W. Klop, J. W. Geus;, *J. Catal.* **1985**, *96*, 2.
[16] C. H. Bartholomew, *Catal. Rev.* **2007**, *24*, 1.
[17] M. C. Annesini, V. Piemonte, L. Turchetti, *Chem. Eng. Trans.* **2007**, *11*.
[18] H. Bengaard, *J. Catal.* **2002**, *209*, 2.
[19] J. P. Coad, J. C. Rivière, *Surf. Sci.* **1971**, *25*, 3.
[20] P. B. Tøttrup, *J. Catal.* **1976**, *42*.
[21] J. R. Rostrup-Nielsen, J. Sehested, in *Stud. Surf. Sci. Catal.* (Eds.: J.J. Spivey, G.W.

Roberts, B.H. Davi), Elsevier, **2001**, pp. 1–12.
[22] W. Li, Y. Shi, Y. Luo, Y. Wang, N. Cai, *J. Power Sources* **2015**, *276*.
[23] C. M. Finnerty, N. J. Coe, R. H. Cunningham, R. M. Ormerod, *Catal. Today* **1998**, *46*, 2–3.
[24] M. Ito, T. Tagawa, S. Goto, *Appl. Catal. A Gen.* **1999**, *177*, 1.
[25] V. Subotić, C. Schluckner, J. Mathe, J. Rechberger, H. Schroettner, C. Hochenauer, *J. Power Sources* **2015**, *295*.
[26] S. D. Ebbesen, M. Mogensen, *J. Power Sources* **2009**, *193*, 1.
[27] J. Aicart, F. Usseglio-Viretta, J. Laurencin, M. Petitjean, G. Delette, L. Dessemond, *Int. J. Hydrogen Energy* **2016**, *41*, 39.
[28] C. Graves, S. D. Ebbesen, M. Mogensen, *Solid State Ionics* **2011**, *192*, 1.
[29] Y. Shi, Y. Luo, N. Cai, J. Qian, S. Wang, W. Li, H. Wang, *Electrochim. Acta* **2013**, *88*.
[30] I. Alstrup, B. S. Clausen, C. Olsen, R. H. H. Smits, J. R. Rostrup-Nielsen, in *Stud. Surf. Sci. Catal.* (Ed.: A. Parmaliana et al), Elsevier Science, **1998**, pp. 5–14.
[31] P. Fan, X. Zhang, D. Hua, G. Li, *Fuel Cells* **2016**.
[32] K. Sasaki, Y. Teraoka, *J. Electrochem. Soc.* **2003**, *150*, 7.
[33] J.-W. Snoeck, G. F. Froment, M. Fowles, *Ind. Eng. Chem. Res.* **2002**, *41*, 17.
[34] S. Primdahl, M. Mogensen, *J. Electrochem. Soc.* **1997**, *144*, 10.
[35] S. B. Adler, *Solid State Ionics* **1998**, *111*, 1–2.
[36] J.-W. Kim, *J. Electrochem. Soc.* **1999**, *146*, 1.
[37] J. D. Duhn, A. D. Jensen, S. Wedel, C. Wix, *J. Power Sources* **2016**, *336*.
[38] M. Ni, *Int. J. Hydrogen Energy* **2012**, *37*, 8.
[39] V. Novaresio, M. García-Camprubí, S. Izquierdo, P. Asinari, N. Fueyo, *Comput. Phys. Commun.* **2012**, *183*, 1.
[40] E. Hern, D. Singh, P. N. Hutton, N. Patel, M. D. Mann, *J. Power Sources* **2004**, *138*.
[41] E. Resch, Numerical and Experimental Characterisation of Convective Transport in Solid Oxide Fuel Cells, Queen's University, Kingston, Ontario, Canada, **2008**.
[42] J. Laurencin, D. Kane, G. Delette, J. Deseure, F. Lefebvre-Joud, *J. Power Sources* **2011**, *196*, 4.
[43] S. . Aruna, M. Muthuraman, K. . Patil, *Solid State Ionics* **1998**, *111*, 1–2.
[44] D. Simwonis, F. Tietz, D. Stover, *Solid State Ionics* **2000**, *132*.
[45] A. Weber, E. Ivers-Tiffée, *J. Power Sources* **2004**, *127*, 1–2.
[46] C. Stoots, J. O'Brien, J. Hartvigsen, *Int. J. Hydrogen Energy* **2009**, *34*, 9.
[47] J. Aicart, M. Petitjean, J. Laurencin, L. Tallobre, L. Dessemond, *Int. J. Hydrogen Energy* **2015**, *40*, 8.
[48] V. Menon, V. M. Janardhanan, O. Deutschmann, *ECS Trans.* **2013**, *57*, 1.
[49] J. Aicart, J. Laurencin, M. Petitjean, L. Dessemond, *Fuel Cells* **2014**, *14*, 3.
[50] J. R. Rostrup-Nielsen, L. J. Christiansen, *Concepts In Syngas Manufacture*, Imperial College Press, London, **2011**.
[51] M. Ni, *J. Power Sources* **2012**, *202*.
[52] R. E. Williford, L. a. Chick, G. D. Maupin, S. P. Simner, J. W. Stevenson, *J. Electrochem. Soc.* **2003**, *150*, 8.
[53] G. Brus, K. Miyawaki, H. Iwai, M. Saito, H. Yoshida, *Solid State Ionics* **2014**, *265*.
[54] Y. Shi, C. Li, N. Cai, *J. Power Sources* **2011**, *196*, 13.
[55] W. Li, H. Wang, Y. Shi, N. Cai, *Int. J. Hydrogen Energy* **2013**, *38*.
[56] G. Hawkes, J. O'Brien, C. Stoots, B. Hawkes, *Int. J. Hydrogen Energy* **2009**, *34*, 9.
[57] G. Hawkes, J. O'Brien, C. Stoots, S. Herring, M. Shahnam, *Heat Transf. Vol. 4* **2005**.
[58] W. Li, Y. Shi, Y. Luo, N. Cai, *J. Power Sources* **2013**, *243*.
[59] Y. Elesin, M. F. Madsen, T. K. Petersen, *Proc. 11th Eur. SOFC SOEC Forum 2014* **2014**, July.

[60] M. W. Chase Jr, in *J. Phys. Chem. Ref. Data, Monogr. 9*, **1998**, pp. 1–1951.
[61] A. Leonide, S. Hansmann, E. Ivers-Tiffée, *ECS Trans.* **2010**, *28*, 11.
[62] J. Laurencin, F. Lefebvre-Joud, G. Delette, *J. Power Sources* **2008**, *177*, 2.
[63] T. Kawashima, M. Hishinuma, *Mater. Trans. Jim* **1996**, *37*, 9.
[64] K. W. Schlichting, N. P. Padture, P. G. Klemens, *J. Mater. Sci.* **2001**, *36*, 12.
[65] B. Todd, J. B. Young, *J. Power Sources* **2002**, *110*, 1.
[66] S. Paydar, M. H. Shariat, S. Javadpour, *Int. J. Hydrogen Energy* **2016**.